

In Situ SEM Observations of Fracture Behavior of Laser Welded–Brazed Al/Steel Dissimilar Joint

Hongbo Xia, Caiwang Tan, Liqun Li, and Ninshu Ma

(Submitted June 25, 2017; in revised form January 30, 2018; published online February 16, 2018)

Laser welding–brazing of 6061-T6 aluminum alloy to DP590 dual-phase steel with Al-Si12 flux-cored filler wire was performed. The microstructure at the brazing interface was characterized. Fracture behavior was observed and analyzed by in situ scanning electron microscope. The microstructure of the brazing interface showed that inhomogeneous intermetallic compounds formed along the thickness direction, which had a great influence on the crack initiation and propagation. In the top region, the reaction layer at the interface consisted of scattered needle-like $\text{Fe}(\text{Al},\text{Si})_3$ and serration-shaped $\text{Fe}_{1.8}\text{Al}_{7.2}\text{Si}$. In the middle region, the compound at the interface was only serration-shaped $\text{Fe}_{1.8}\text{Al}_{7.2}\text{Si}$. In the bottom region, the interface was composed of lamellar-shaped $\text{Fe}_{1.8}\text{Al}_{7.2}\text{Si}$. The cracks were first detected in the bottom region and propagated from bottom to top along the interface. At the bottom region, the crack initiated and propagated along the $\text{Fe}_{1.8}\text{Al}_{7.2}\text{Si}$ /weld seam interface during the in situ tensile test. When the crack propagated into the middle region, a deflection of crack propagation appeared. The crack first propagated along the steel/ $\text{Fe}_{1.8}\text{Al}_{7.2}\text{Si}$ interface and then moved along the weld seam until the failure of the joint. The tensile strength of the joint was 146.5 MPa. Some micro-cracks were detected at $\text{Fe}(\text{Al},\text{Si})_3$ and the interface between the steel substrate and $\text{Fe}(\text{Al},\text{Si})_3$ in the top region while the interface was still connected.

Keywords crack initiation and propagation, Fe/Al dissimilar joint, laser welding–brazing, microstructure

1. Introduction

The use of a steel/Al dissimilar joint is now increasingly popular in the automotive industry due to its light weight, low cost, and combination of hybrid mechanical properties (Ref 1, 2). In the joining of steel/Al dissimilar joint, many different welding methods have been adopted to obtain a suitable weld seam, such as solid-phase welding (Ref 3, 4), brazing (Ref 5), fusion welding (Ref 6), and welding–brazing (Ref 7–9). Laser welding–brazing shows great advantages over other welding techniques due to its lower inhomogeneous intermetallic compound (IMC) thickness, flexible energy control, and accurate melting location. In laser welded–brazed steel/Al dissimilar joints, inhomogeneous IMCs are formed at the steel interface along the thickness direction due to the large temperature gradient.

Zhang et al. (Ref 10) observed different IMC morphologies along the steel interface in the top and bottom regions in a laser welded–brazed 1.2-mm H220YD/6061 dissimilar butt joint. A 13- μm continuous thick layer and a scattered bar were found at the interface at the upper part of the joint, and a 5- μm thin layer

was found at the lower part. Ozaki et al. (Ref 11) also observed different IMC morphologies in the steel interface during the laser roll welding–brazing of a GI/A6000 dissimilar lap joint. They found that the IMC located at the center of the laser spot was much thicker (13 μm) than was that at the edge (4.1 and 4.9 μm). According to previous studies (Ref 12–14), Fe–Al IMCs are brittle, and their morphology, thickness, and distribution have great effects on the final tensile strength of the joint.

To obtain a qualified joint, the influence of IMCs on the fracture behavior needs to be investigated. In situ scanning electron microscope (SEM) could provide a dynamic observation of crack initiation and propagation. Chen et al. (Ref 15) investigated the initiation and propagation of cracks in different IMCs in a laser welded–brazed Ti/Al dissimilar butt joint. They reported that lamellar-, serration-, and cellular-shaped IMC all possessed good advantages for the final tensile strength. Qiu et al. (Ref 16) studied the initiation and propagation of cracks in a Fe/Al dissimilar lap joint by resistance spot welding. They found that the crack propagated in the IMC and aluminum but that its propagation was arrested in the interface between IMC and steel. Nevertheless, the initiation and propagation of cracks in inhomogeneous Fe–Al IMCs along the steel interface in the thickness direction in a laser welded–brazed steel/Al dissimilar butt joint have rarely been reported.

In this work, laser welding–brazing of 6060-T6 aluminum alloy to DP590 dual-phase steel using Al-Si12 flux-cored filler wire was performed. The purpose of this research was to investigate the microstructure and fracture behavior of the laser welded–brazed 2-mm-thick DP590/6061 dissimilar butt joint. The crack initiation and propagation were monitored by in situ SEM observations, and the influence of different IMCs on the fracture behavior of DP590/6061 dissimilar butt joint was discussed. The research findings provide a reference to achieve a reliable joint by further optimizing the IMC morphology.

Hongbo Xia and **Liqun Li**, State Key Laboratory of Advanced Welding and Joining, Harbin Institute of Technology, 92 West Dazhi Street, Harbin 15001, China; **Caiwang Tan**, State Key Laboratory of Advanced Welding and Joining, Harbin Institute of Technology, 92 West Dazhi Street, Harbin 15001, China; and Shandong Provincial Key Laboratory of Special Welding Technology, Harbin Institute of Technology at Weihai, Weihai 264209, China; and **Ninshu Ma**, Joining and Welding Research Institute, Osaka University, 11-1 Mihogaoka, Ibaraki, Osaka 567-0047, Japan. Contact e-mails: tancaiawang@hitwh.edu.cn and liliquan@hit.edu.cn.

2. Experimental Procedure

2.1 Selected Materials

In this work, commercially DP590 and 6061-T6 sheets with similar dimension of 100 mm × 50 mm × 2 mm were selected as the base metals. The flux-cored (KAlF₄ and K₃AlF₆ eutectic) filler wire of Al-Si12 with the diameter of 1.4 mm was selected, which can protect the molten filler from the oxidation, clean the contamination left on the steel interface, and hence improve the wetting ability of the molten filler wire. The chemical compositions and tensile strength of the base metals and filler wire (Al-Si12) were listed in Table 1.

2.2 Laser Welding–Brazing Process

Figure 1 shows the schematic diagram of laser welding–brazing of Al to steel. Filler wire was melted by a continuous wave fiber laser with a maximum power of 6 kW (IPG YLR-6000). To enhance the heat dissipation of the joint, a Cu-base backing block was added. Double shielding argon gas system was adopted to prevent molten filler wire from oxidation. Besides, 45° grooves shape was cut in DP590 and 6061 sheets to make the molten filler metal spread along the brazing interface more sufficiently. The filler wire was fed in front of welding direction to keep the molten filler metal flow into the molten pool more stable. The detailed welding–brazing parameters are listed in Table 2.

2.3 In Situ Observation

After laser welding–brazing process, in situ tensile specimens with 1 mm wide were cut from the joint by a line cut machine. Figure 2 shows the schematic diagram of in situ tensile testing. The reinforcement of the joint was removed to make the in situ tensile test more accurate. The surface to be observed was ground by 200, 400, 800, and 1000 SiC grades and then polished by 1.0- μ m-diameter diamond suspension to obtain a mirror-like surface. Interface of the polished specimen was observed in the scanning electron microscope (SEM FEI Quanta200) during the in situ tensile test process at room temperature. The in situ loading process could be paused at any time to better observe cracks, and SEM images were taken accordingly. To obtain a better observation initiation and propagation of the crack at the interface, a minimum tensile speed (0.5 mm/min) was adopted by the testing machine (INSTRON 1186).

3. Results

3.1 Appearances and Cross Section

Figure 3 shows a typical appearance of a laser welded–brazed DP590 steel/6061-T6 dissimilar joint. A good front and

back appearance formed under the optimized process parameters, as seen in Fig. 3(a) and (b), due to the good wetting of the molten filler metal and stable welding–brazing process. Figure 3(c) shows a cross section of the joint. In Fig. 3(c), molten filler wire spread over the steel interface smoothly, and no obvious defects (such as porosity, unbrazed region, and undercut) were observed in the whole joint at the brazing side.

3.2 IMC Morphology

Under the combined heat of laser irradiation and heat conduction of molten liquid filler, Fe atoms diffused into the liquid filler and react with Al atoms, giving rise to the generation of IMCs at the interface. A large temperature gradient existed along the steel interface in the thickness direction because the laser is a local and rapid heating technology that ultimately provides different IMCs' morphologies from top to bottom. For the sake of discussion, three locations were selected in the steel interface along the thickness direction: A (top), B (middle), and C (bottom) as seen in

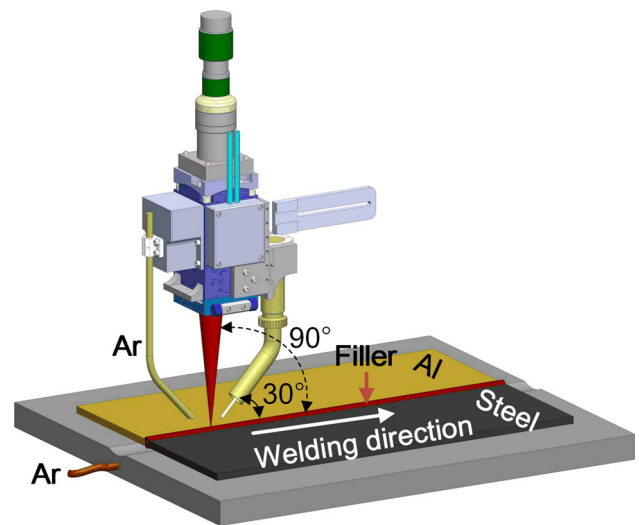


Fig. 1 Schematic diagram of the laser welding–brazing process

Table 2 Detailed laser welding–brazing parameters

Welding parameters	Value
Laser power, W	2200
Defocus distance, mm	+ 40
Distance of laser spot offset to Al side, mm	0.4
Welding speed, m/min	0.5
Feeding speed of filler wire, m/min	3.5
Flowing rate of shielding gas, L/min	20
The angle of between filler wire and workpiece, θ	30°

Table 1 Chemical compositions of base metals and filler metal (wt.%)

	C	Mn	Si	S	P	Fe	Mg	Zn	Cu	Al	Ti	Tensile strength (σ , MPa)
DP590	0.068	1.61	0.447	0.002	3.5–4.5	Bal	590
6061-T6	0.8–1.0	0.15	0.4–0.8	0.7	...	0.25	0.15–0.4	Bal	...	310
Filler	...	0.15	12	0.8	0.1	0.2	0.3	Bal	0.15	210

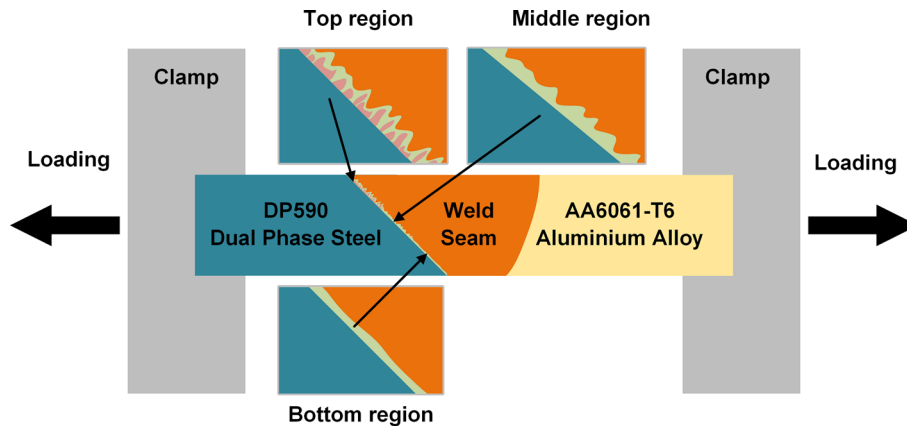


Fig. 2 In situ tensile test sample

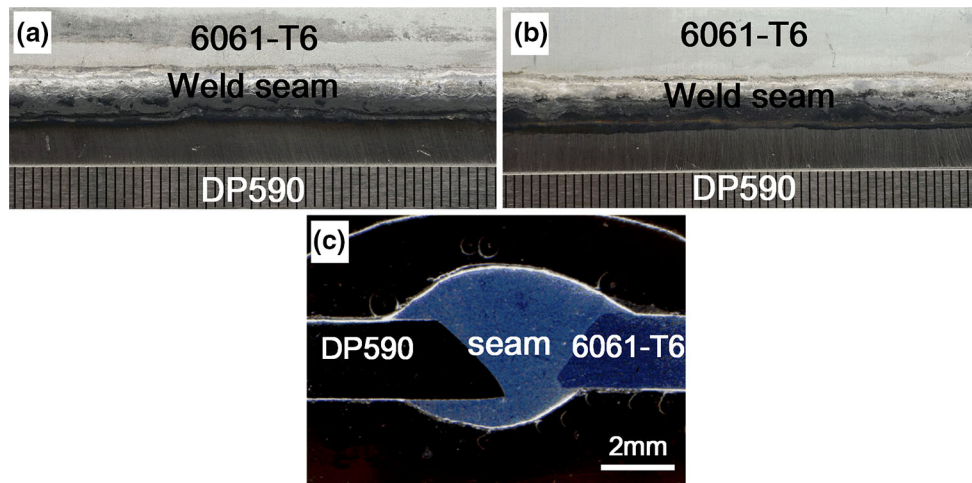


Fig. 3 Appearance and cross section of laser welded–brazed DP590/6060 dissimilar butt joint: (a) front appearance, (b) back appearance, (c) cross-sectional appearance

Fig. 4(a). The interfacial IMCs' morphologies in these regions were observed under the backscattered electron (BSE) mode.

The IMCs in region A were approximately 9 μm , on average, and consisted of two different morphologies, as seen in Fig. 4(b). The IMC adjacent to the steel interface (#1) was needle shaped and mainly entrapped by the IMC near the weld seam (#2). EDS results of IMC #1 indicated that this phase consisted of 23.61 at.% Fe, 72.03 at.% Al, and 03.82 at.% Si (as seen in Fig. 4c), confirming that it was $\text{Fe}(\text{Al},\text{Si})_3$. IMC #2 was continuous serration shaped and inserted toward the weld seam. It was composed of 19.00 at.% Fe, 71.07 at.% Al, and 09.30 at.% Si, which implied that it was $\text{Fe}_{1.8}\text{Al}_{7.2}\text{Si}$ (as seen in Fig. 4d). Because Si has a similar crystal structure to Al, it would be a solid solute in the Fe–Al IMCs, which contributed to the existence of Si in the IMCs (Ref 17).

Figure 5(a) shows the IMC in region B (#3). IMC #3 appeared to be serration shaped, and its thickness was approximately 6 μm . The morphology of IMC #3 was different from that in region A, and no obvious inter-layer boundary was found, indicating that it was composed of only one phase. Its composition was 20.75 at.% Fe, 71.03 at.% Al, and 08.04 at.% Si (as seen in Fig. 5b), which revealed that IMC #3 was $\text{Fe}_{1.8}\text{Al}_{7.2}\text{Si}$.

In region C (as seen in Fig. 5c), IMC #4 was continuous lamella shaped, and its thickness was approximately 1.8 μm . IMC #4 contained a similar composition as IMC #2 and IMC #3, i.e., 19.26 at.% Fe, 73.88 at.% Al, and 06.75 at.% Si (seen in Fig. 5d), suggesting that IMC #4 was $\text{Fe}_{1.8}\text{Al}_{7.2}\text{Si}$.

From region A to region C, the morphologies of IMCs were different, and their thickness values decreased. According to previous research (Ref 18, 19), the peak temperature at the brazing side, which determines the morphology of IMCs, in the top region was higher than that in the bottom region due to the former's shorter distance to the laser spot center, which resulted in inhomogeneous IMCs along the steel interface.

4. In Situ Tensile Observation

To clarify the influence of the IMCs' morphologies on the fracture behavior of the interface, an in situ tensile test was carried out to observe the initiation and propagation of a crack in the interface. The load–displacement curve of the in situ tensile test is plotted in Fig. 6. Crack initiation was first observed in region C, where the interface was joined by a 1.8-

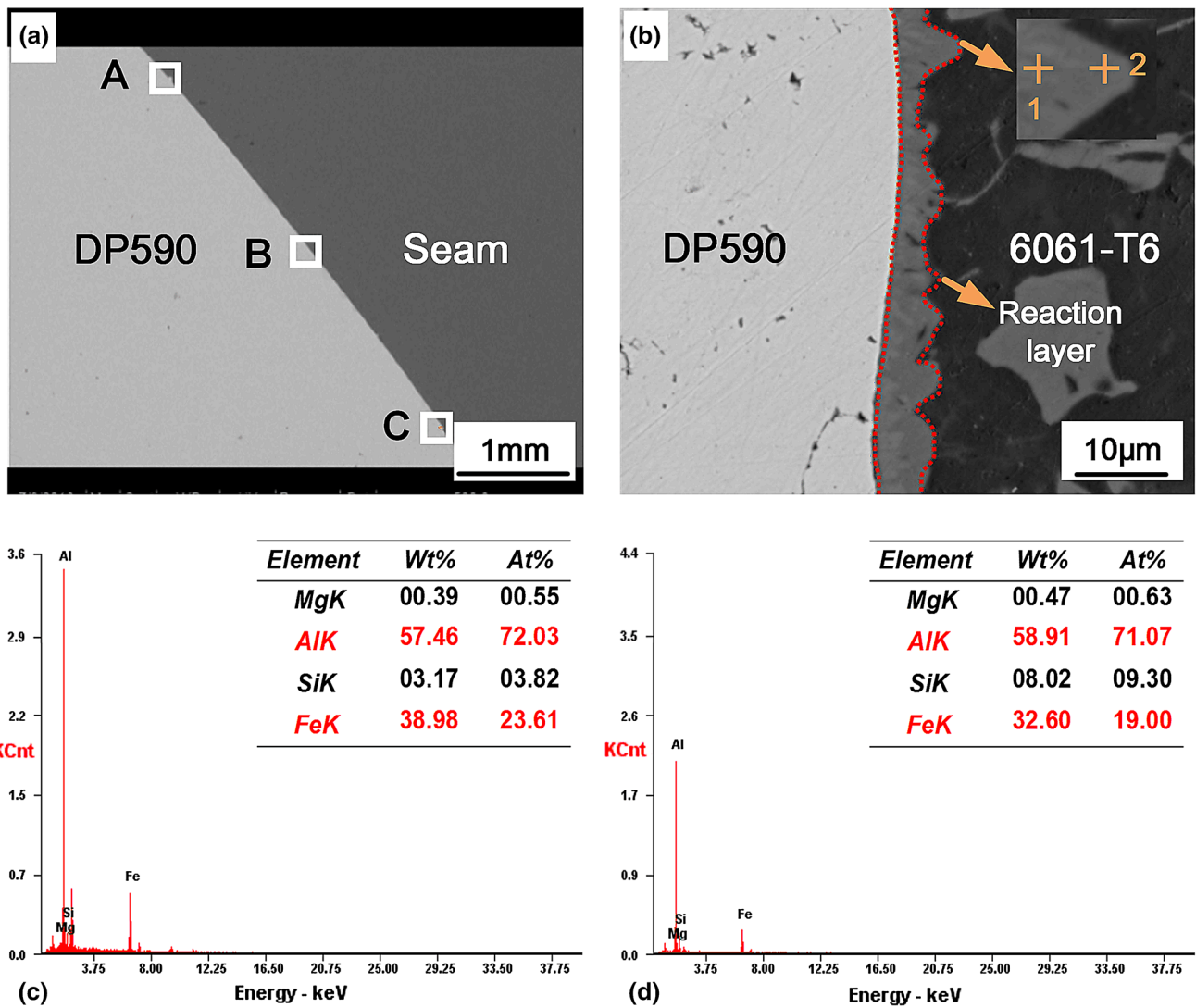


Fig. 4 Interfacial microstructure and phase composition in region A: (a) selected locations, (b) IMC morphology in region A, (c) EDS results of IMC #1 in region A, (d) EDS results of IMC #2 in region A

μm lamella-shaped $Fe_{1.8}Al_{7.2}Si$, as seen in Fig. 5(c). Crack I initiated at the interface between the $Fe_{1.8}Al_{7.2}Si$ layer and the weld seam and propagated along this interface (as seen in Fig. 7a). With the proceeding of the in situ tensile test, crack I became larger and crack II was detected at the lower location as seen in Fig. 7(b). These two cracks became larger and finally propagated together, which resulted in the fracture of the interface, as seen in Fig. 7(c). This process corresponded to stage 1 in Fig. 6. The fractured surface close to the weld seam can be seen in Fig. 7(d). The values of 19.59 at.% Fe, 73.06 at.% Al, and 7.35 at.% Si in region 5 (as seen in Fig. 7e) and 0.093 at.% Fe, 80.95 at.% Al, and 17.54 at.% Si in region 6 (as seen in Fig. 7f) revealed that the components of these two regions were $Fe_{1.8}Al_{7.2}Si$ and residual filler metal, respectively. Many micro-tear ridges and dimples induced by the fracture of $Fe_{1.8}Al_{7.2}Si$ and the weld seam were found at the fractured surface, which showed that the fracture in this region was a ductile fracture. From Fig. 6, step 1 was finished when the tensile load was approximately 160 N (80 MPa). In fact, the interface joined by this morphology was higher than 80 MPa because a large residual stress aggregated in this region due to

the geometric shape of the groove corner. The existing stress served as pre-tensile stress before the actual tensile load was carried out.

When the crack propagated from region C to region B, different initiation and propagation behaviors were observed. In this region, the interface was joined with serration-shaped $Fe_{1.8}Al_{7.2}Si$ and two main cracks (cracks III and IV) existed in the interface, as seen in Fig. 8(a) and (b). Crack III propagated from the bottom of region C, whereas crack IV was newly generated in the interface between the steel substrate and $Fe_{1.8}Al_{7.2}Si$. In addition, many second cracks were also observed at the $Fe_{1.8}Al_{7.2}Si$ layer, as seen in Fig. 8(c). These second cracks also initiated at the steel/ $Fe_{1.8}Al_{7.2}Si$ interface and propagated through this IMC layer toward the weld seam. As the in situ tensile load continued, cracks III and IV became larger and finally met. Then, an alternation of the crack propagation direction occurred, which turned from the steel/ $Fe_{1.8}Al_{7.2}Si$ interface to the weld seam, as shown in Fig. 8(c) and (d). The fractured interface at the steel side is presented in Fig. 8(e). The residual IMCs were $Fe_{1.8}Al_{7.2}Si$, according to the EDS results. This process was also reflected in the load–

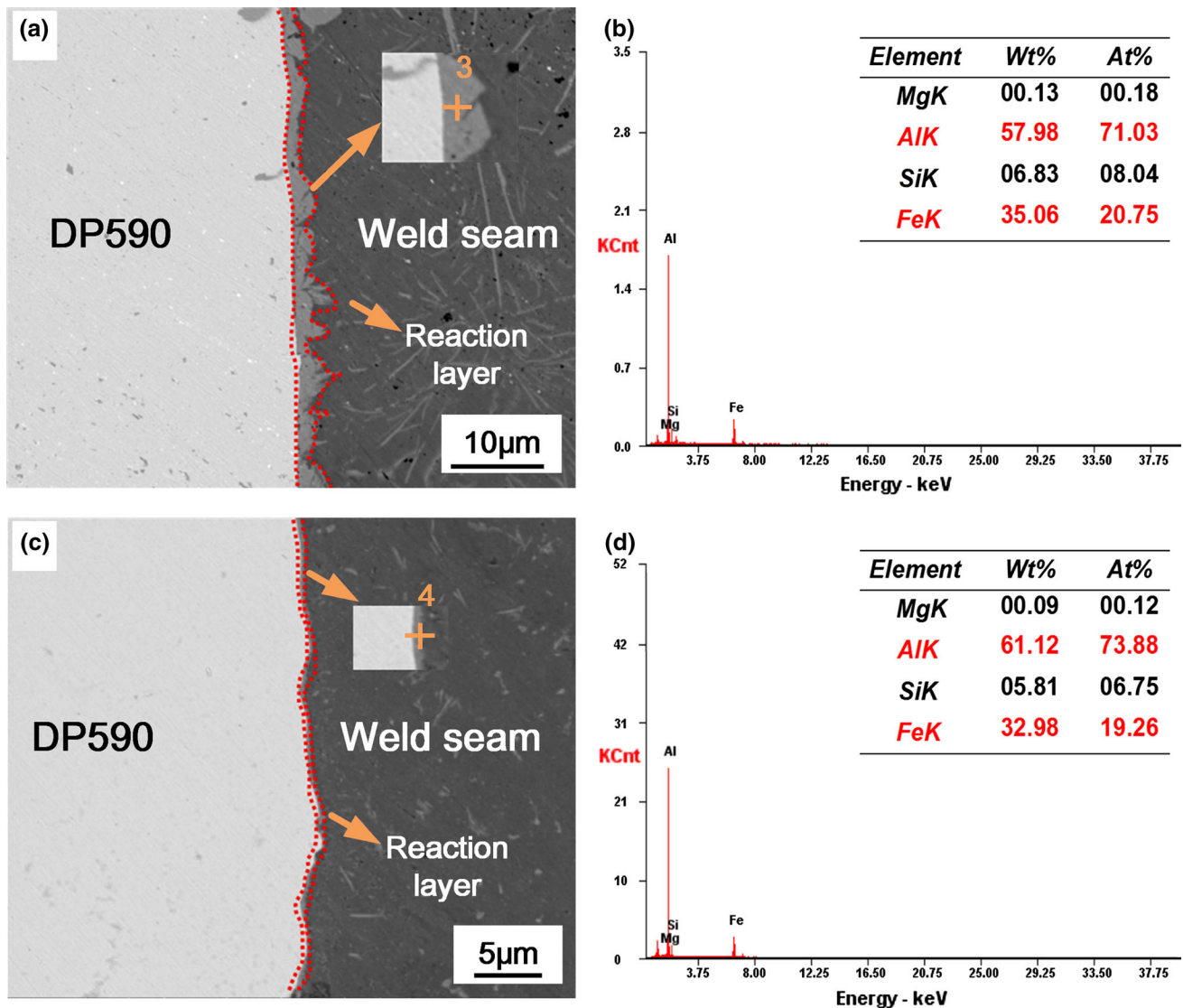


Fig. 5 Interfacial microstructure and phase compositions in regions B and C: (a) IMC morphology in region B, (b) EDS results of IMC #3 in region B, (c) IMC morphology in region C, (d) EDS results of IMC #4 in region C

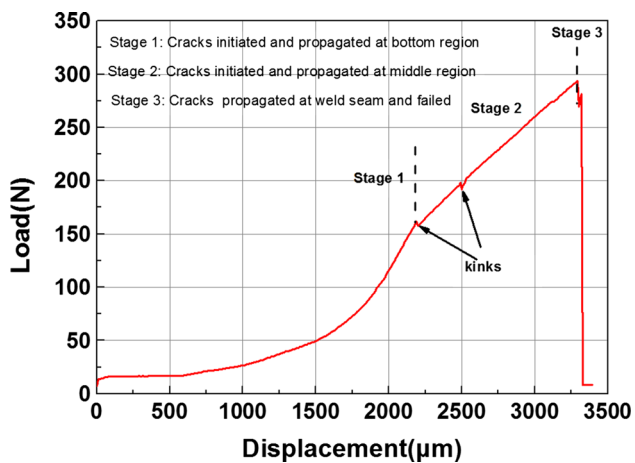


Fig. 6 Load–displacement curve of the in situ tensile test

displacement curve (stage 2 of Fig. 6). It was observed that in this stage, the curve increased sharply when the crack propagated from the bottom of region C to the middle of region B. In addition, some kinks could be found in stage 2 of the load–displacement curve, which was an indication of new crack generation (Ref 20). The presence of kinks in stage 2 showed good consistency with the observation of crack behavior in Fig. 8(b). The crack deflection in the middle region revealed that the interface joined by the serration-shaped $\text{Fe}_{1.8}\text{Al}_{7.2}\text{Si}$ could prevent the cracks from propagating along the steel/ $\text{Fe}_{1.8}\text{Al}_{7.2}\text{Si}$ interface.

When the load reached 293 N (146.5 N/mm failed strength divided by the area of tested sample, as seen in stage 3 of Fig. 6), the crack rapidly propagated into the weld seam and joint fracture occurred instantaneously, as seen in Fig. 8(d) and 9(a). When the tensile test ended, only some discontinuous micro-cracks were observed at the interface between $\text{Fe}(\text{Al},\text{Si})_3$ and both the steel substrate (as seen in Fig. 9(b) and $\text{Fe}(\text{Al},\text{Si})_3$

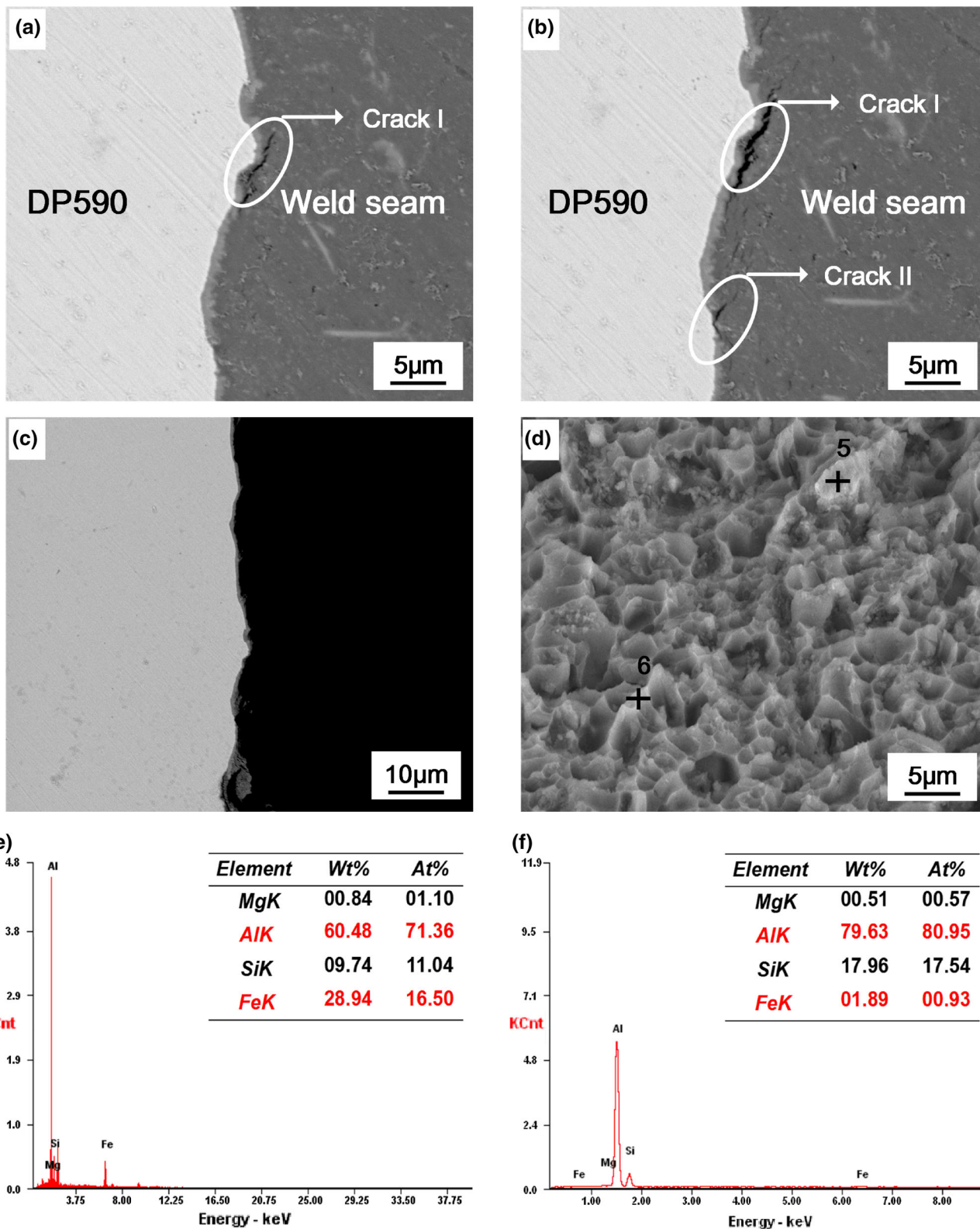


Fig. 7 Fracture behavior in region C: (a) crack initiation, (b) new crack initiation, (c) fractured interface, (d) fractured interface at weld seam side, (e) EDS results in region 5, (f) EDS results in region 6

substrate. Although the IMC thickness in this region was larger than that in regions B and C, the 9-µm continuous segregated needle-shaped $\text{Fe}(\text{Al},\text{Si})_3$ + serration-shaped $\text{Fe}_{1.8}\text{Al}_{7.2}\text{Si}$ was acceptable for the interface in the top region.

To better reveal the repeatability of the above in situ tensile results, an extra in situ observation was performed on a joint with reinforcement obtained under the same welding–brazing parameters. The corresponding results are listed in Fig. 10.

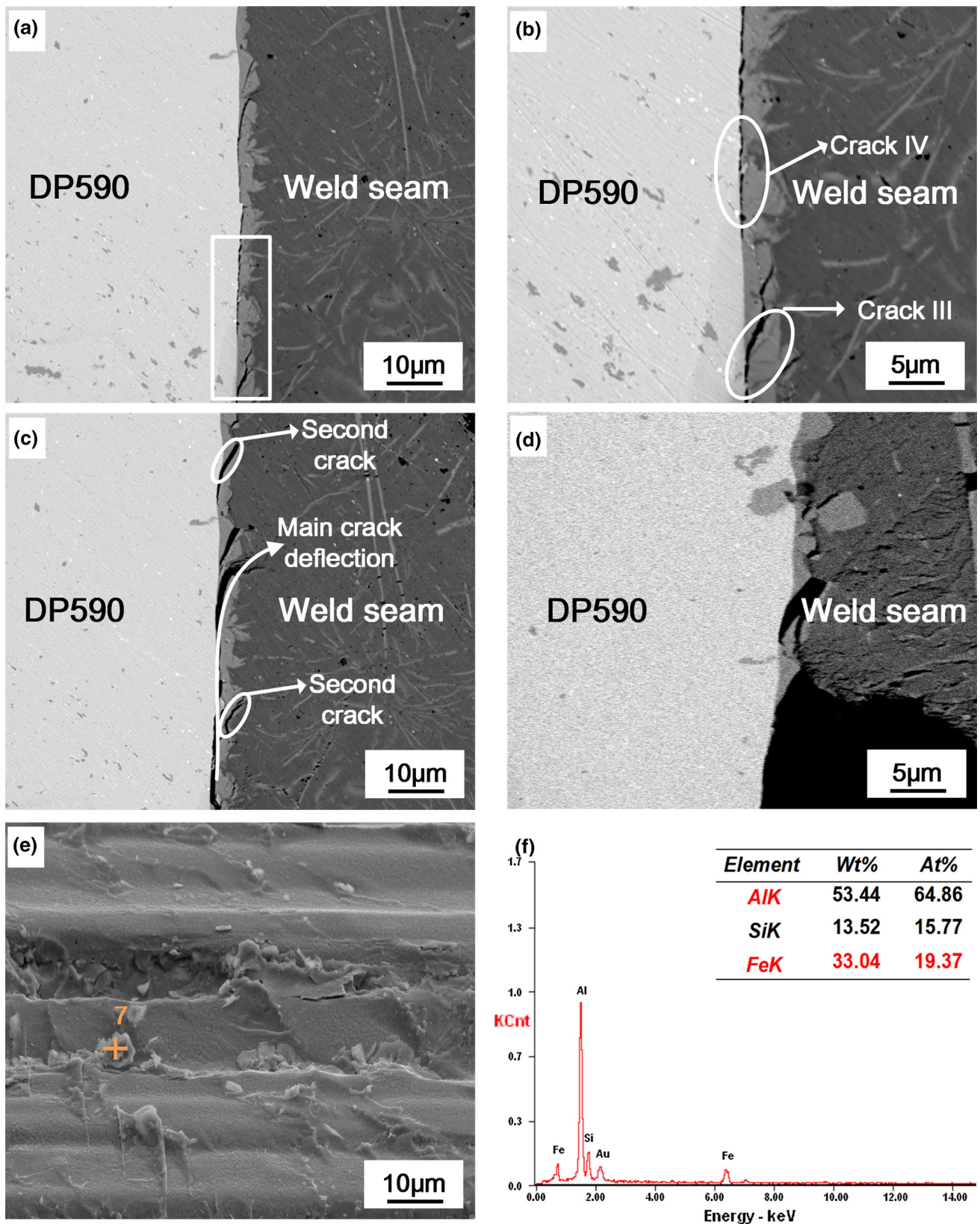


Fig. 8 Fracture behavior in region B: (a) crack initiation, (b) amplification of the rectangle region in a, (c) crack deflection, (d) fractured interface, (e) fractured interface at Al side, (f) EDS results in region 7 in (e)

From Fig. 10(a), it could be found that the fracture load was 352 N ($352 \text{ N}/2 \text{ mm}^2 = 176 \text{ MPa}$), which was higher than the tensile results given in Fig. 6 due to the existence of reinforcement. Kink was also detected in stage 2, which was consistent with the results plotted in Fig. 6. The fracture path of the joint is demonstrated in Fig. 10(b), and the partial interface + weld seam fractured model was the same as the result illustrated in Fig. 9(a). In addition, the origination of cracks in the bottom region, where the interface was connected to thin-layer $\text{Fe}_{1.8}\text{Al}_{7.2}\text{Si}$, the deflections of the cracks in the middle region, where the interface was composed of serrated $\text{Fe}_{1.8}\text{Al}_{7.2}\text{Si}$, and the appearance of micro-cracks in the $\text{Fe}(\text{Al},\text{Si})_3/\text{weld seam}$ interface were all in good correspondence to the results plotted in Fig. 7, 8, and 9.

5. Discussion

An eligible DP590/6061-T6 dissimilar butted joint with good appearance was obtained by laser welding–brazing technology with AlSi12 filler wire, which can expand its application in the automobile industry. Because the laser was a local heat technology, uneven IMCs formed along the steel interface in the thickness direction due to the large temperature gradient. From the above experimental results, these uneven IMCs had a great influence on the initiation and propagation of cracks, which finally determined the fracture behavior of the joint.

The cracks first initiated at the bottom region of the joint, where the interface was mainly connected by lamella-shaped $\text{Fe}_{1.8}\text{Al}_{7.2}\text{Si}$. It was closely associated with one key factor: stress concentration. When the laser welding–brazing process was finished, residual stress was generated at the interface as a result of the large difference in the thermal expansion between DP590 ($12.5 \times 10^{-6} \text{ }^\circ\text{C}^{-1}$) and 6061-T6 ($23.45 \times 10^{-6} \text{ }^\circ\text{C}^{-1}$). According to previous research (Ref 21), the residual stress at the bottom of the groove was larger than that both at the top and in the vicinity. Meanwhile, the sharp angle of the groove being located at the bottom of the joint would contribute to a stronger stress concentration. Generally, a lower heat input could lead to a lower interfacial residual stress. However, when the interfacial residual stress was reduced to an acceptable level by employing a lower heat input, the interfacial IMC might be insufficient, which would also be detrimental to the interfacial

bonding strength (Ref 15). When the cracks were first observed at the bottom region, there were five possible locations where they could be initiated: Fe substrate, weld seam, $\text{Fe}_{1.8}\text{Al}_{7.2}\text{Si}$ layer, interface of steel/ $\text{Fe}_{1.8}\text{Al}_{7.2}\text{Si}$ and $\text{Fe}_{1.8}\text{Al}_{7.2}\text{Si}/\text{weld seam}$. Since steel and IMC had higher tensile strengths than did the filler metal, it was impossible for a crack to initiate at these regions. Second, if cracks initiated at the steel/ $\text{Fe}_{1.8}\text{Al}_{7.2}\text{Si}$ interface or the lamella-shaped $\text{Fe}_{1.8}\text{Al}_{7.2}\text{Si}$ layer, plastic deformation would occur at the Fe substrate and $\text{Fe}_{1.8}\text{Al}_{7.2}\text{Si}$ near the crack tip due to the thin $\text{Fe}_{1.8}\text{Al}_{7.2}\text{Si}$ layer, which would lead to a sharp increase in deformation energy. Based on the above analysis results, it was safely concluded that cracks would not be initiated at the Fe substrate, lamella-shaped IMC, or interface between steel and IMC. Third, many micro-tear ridges and dimples induced by the fractured weld seam were found at the fractured surface, as shown in Fig. 7(d), which indicated that the cracks mainly initiated in and propagated along the $\text{Fe}_{1.8}\text{Al}_{7.2}\text{Si}/\text{weld seam}$ interface.

Serration-shaped $\text{Fe}_{1.8}\text{Al}_{7.2}\text{Si}$ in the interface could prevent crack propagation along the interface between the steel substrate and $\text{Fe}_{1.8}\text{Al}_{7.2}\text{Si}$ layer. In this stage, the tensile stress in front of the crack tips became higher, with crack propagation resulting from the larger moment of force with enlargement distance between the load position and crack tip. Compared with lamella-shaped $\text{Fe}_{1.8}\text{Al}_{7.2}\text{Si}$, a larger contacting interfacial area could be provided by serration-shaped $\text{Fe}_{1.8}\text{Al}_{7.2}\text{Si}$, and more plastic energy would be consumed during crack propagation. Although the thickness of serration-shaped $\text{Fe}_{1.8}\text{Al}_{7.2}\text{Si}$ was larger than that of lamella-shaped $\text{Fe}_{1.8}\text{Al}_{7.2}\text{Si}$, the larger interfacial area and good plasticity of the weld seam could release the residual stress at the interface. In addition, secondary cracks, as seen in Fig. 8(c), that originated at the interface between the steel substrate $\text{Fe}_{1.8}\text{Al}_{7.2}\text{Si}$ layer and arrested at the interface between the $\text{Fe}_{1.8}\text{Al}_{7.2}\text{Si}$ layer and weld seam exerted a certain effect on stress relief. The larger bonding area by serration-shaped $\text{Fe}_{1.8}\text{Al}_{7.2}\text{Si}$, the lower stress concentration, and the inducement of second cracks were attributed to the crack's deflection. Therefore, the interface joined by serration-shaped IMC was acceptable. Chen et al. (Ref 15) also found that serration-shaped (less than $10 \mu\text{m}$) Ti–Al IMC could cause the crack propagation to experience a deflection in the laser welding–brazing of a Ti6Al4V and 5A06 dissimilar joint.

It should be noticed that the comparison of interfacial microstructure in the top region between before and after in situ

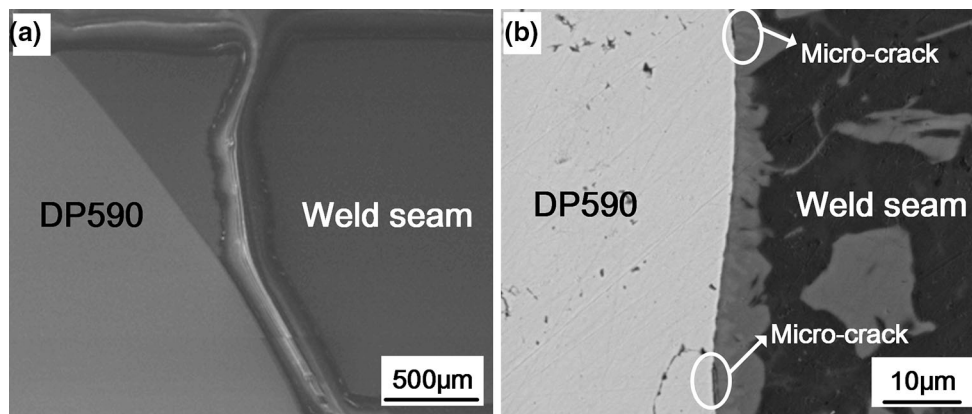


Fig. 9 Morphology of fractured joint: (a) whole fractured joint, (b) region A after in situ tensile test

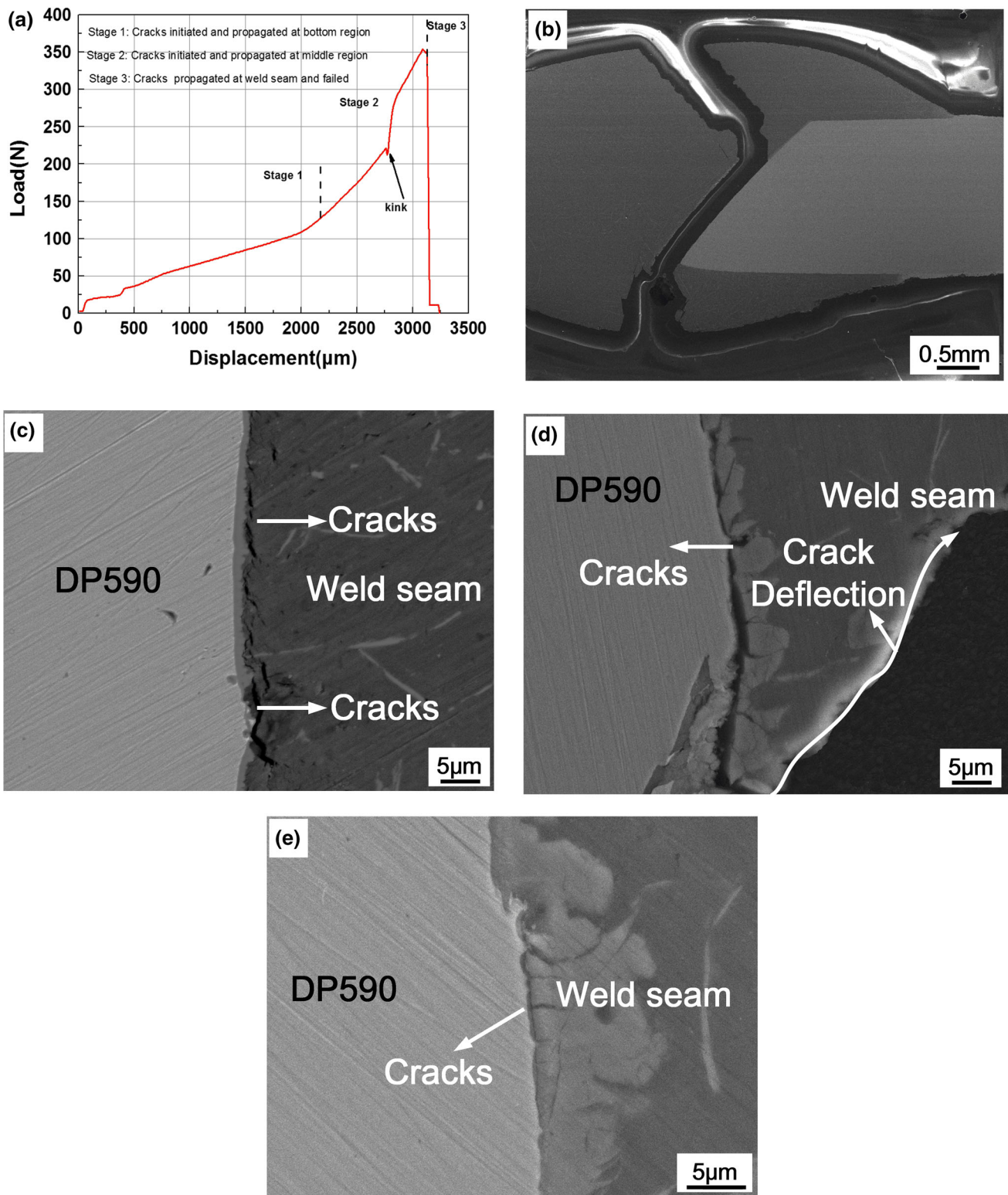


Fig. 10 Repeated in situ tensile experiment: (a) in situ tensile curves, (b) fractured joint, (c) cracks initiations in region C, (d) crack deflection in region B, (e) micro-cracks in region A when the in situ tensile test was finished

tensile test (as seen in Fig. 4b and Fig. 9b) illuminated the improved resistance to crack propagation. Cracks located at the interface between $\text{Fe}(\text{Al},\text{Si})_3$ and Fe substrate and $\text{Fe}(\text{Al},\text{Si})_3$ substrate, rather than $\text{Fe}_{1.8}\text{Al}_{7.2}\text{Si}$, revealed that serration-shaped $\text{Fe}_{1.8}\text{Al}_{7.2}\text{Si}$ possessed a stronger ability to restrain crack

propagation than did the needle-shaped $\text{Fe}(\text{Al},\text{Si})_3$. This result indicated that a high tensile strength joint could be reached by serration-shaped $\text{Fe}_{1.8}\text{Al}_{7.2}\text{Si}$ by controlling the heat input (Ref 22). In addition, the thickness of the IMC should be controlled and less than 10 μm (Ref 23). During the tensile load process,

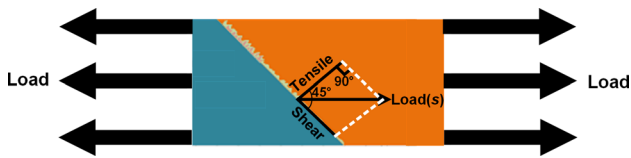


Fig. 11 Schematic diagram of stress distribution for IMC during tensile load

the deflection of crack propagation and relatively strong bonding strength of the interface provided by segregated needle-shaped $\text{Fe}(\text{Al},\text{Si})_3$ + serration-shaped $\text{Fe}_{1.8}\text{Al}_{7.2}\text{Si}$ resulted in the fracture location in Fig. 9(a).

The interfacial IMC was subject to two component forces: tensile stress σ and shear stress τ , as illustrated in Fig. 11. The shear stress τ was responsible for the fracture of IMC along the direction vertical to the brazing interface, and the tensile stress σ was responsible for the fracture of the interface (IMC–steel substrate or IMC–weld seam). In region C, the fracture occurred at the interface between IMC and weld seam. The residual dimples in Fig. 7(a) showed that the tensile stress σ was the main reason for crack initiation and propagation in region C. In region B, the crack initiation and propagation first appeared at the interface between IMC and steel substrate, as noted in Fig. 8(a). This indicated that the tensile stress σ was still the main reason for crack initiation and propagation at this step. Nevertheless, the direction of crack propagation suffered an alteration (vertical to the brazing interface as seen in Fig. 8c) with the process of the tensile load. Thus, the main reason for crack initiation and propagation was changed from the tensile stress σ to the shear stress τ . In region A, only a few microcracks were detected in the interface between IMC and steel substrate. This indicated that the tensile stress σ was the main reason for crack initiation in this region.

The IMC morphology and interfacial residual stress depended mainly on the thermal cycle history along the brazing interface. The appropriate IMC morphologies and a lower interfacial residual stress, which were achieved by controlling heat input, could both favor an excellent joint with high tensile strength. With the further development of laser process technology, various laser heat sources, such as dual-spot or rectangle-spot laser beams, provide many possibilities for controlling the thermal cycle history.

6. Conclusion

6061-T6 aluminum alloy and DP590 dual-phase steel were successfully joined with flux-cored filler wire by laser welding–brazing technology. The microstructure and fracture behavior of the joint were analyzed, and the conclusions are listed as follows:

1. Inhomogeneous IMC distribution along the steel interface in the thickness direction was observed due to different peak temperatures. In the top region, the IMCs' morphologies were needle shaped + continuous serration shaped. The needle-shaped IMC adjacent to the steel interface was $\text{Fe}(\text{Al},\text{Si})_3$, and the continuous serration-shaped IMC closed to the weld seam was $\text{Fe}_{1.8}\text{Al}_{7.2}\text{Si}$. In the middle region, the IMC morphology was serration

shaped, and it contained only $\text{Fe}_{1.8}\text{Al}_{7.2}\text{Si}$. In the bottom region, the IMC morphology was lamella-shaped, and its component was $\text{Fe}_{1.8}\text{Al}_{7.2}\text{Si}$. Their thickness experienced a decrease from top to bottom (9, 6, 1.8 μm).

2. The IMC morphology and residual stress were responsible for crack initiation and propagation at the $\text{Fe}_{1.8}\text{Al}_{7.2}\text{Si}$ /weld seam interface in the bottom region. The fractured surface showed that the interface joined by lamella-shaped $\text{Fe}_{1.8}\text{Al}_{7.2}\text{Si}$ was acceptable. When the crack propagated into the middle region, the propagation direction experienced a deflection. The crack propagated first along the steel/ $\text{Fe}_{1.8}\text{Al}_{7.2}\text{Si}$ interface and then changed to the weld seam until the fracture of the joint, but the IMC in the top region showed little variation. This result suggested that serration-shaped $\text{Fe}_{1.8}\text{Al}_{7.2}\text{Si}$ could prevent the crack from propagating along the steel/IMC interface and that the needle-shaped $\text{Fe}(\text{Al},\text{Si})_3$ + serration-shaped $\text{Fe}_{1.8}\text{Al}_{7.2}\text{Si}$ in the top region (less than 10 μm) exerted little influence on the fracture behavior of the joint.

Acknowledgment

The research was financially supported by National Natural Science Foundation of China (Grant No. 51504074), Key Research and Development Program in Shandong Province (Grant Nos. 2017GGX30147 and 2017CXGC0811), and China Postdoctoral Science Special Foundation (2016T90280).

References

1. Y. Zheng, J.H. Huang, W. Gao et al., Combined Effects of MIG and TIG Arcs on Weld Appearance and Interface Properties in Al/Steel Double-Sided Butt Welding-Brazing, *J. Mater. Process. Technol.*, 2017, **250**, p 25–34
2. M. Masoud, N. Yazdian, H.P. Wang et al., Effect of Filler Wire Composition on Performance of Al/Galvanized Steel Joints by Twin Spot Laser Welding-Brazing Method, *J. Manuf. Process.*, 2018, **31**, p 20–34
3. Y. Yu, H.H. Ma, K. Zhao et al., Study on Underwater Explosive Welding of Al-Steel Coaxial Pipes, *Cent. Eur. J. Energ. Mater.*, 2017, **14**(1), p 251–265
4. P. Joaquin, M. Svoboda, G. Hernan et al., Tool Geometry Optimization in Friction Stir Spot Welding of Al-Steel Joints, *J. Manuf. Process.*, 2017, **26**, p 142–154
5. J.L. Yang, S.B. Xue, P. Xue et al., Development of Zn-15Al-xZr Filler Metals for Brazing 6061 Aluminum Alloy to Stainless Steel, *Mater. Sci. Eng., A*, 2016, **651**, p 425–434
6. J. Yang, Y. Li, H. Zhang et al., Microstructure and Mechanical Properties of Pulsed Laser Welded Al/Steel Dissimilar Joint, *Trans. Nonferrous Met. Soc. China*, 2016, **26**, p 994–1002
7. M. Masoud, Y. Nima, Y. Guang et al., Effect of Dual Laser Beam on Dissimilar Welding-Brazing of Aluminum to Galvanized Steel, *Opt. Laser Technol.*, 2018, **98**, p 214–228
8. J.H. Sun, J. Huang, Q. Yan et al., Fiber Laser Butt Joining of Aluminum to Steel Using Welding-Brazing Method, *Int. J. Adv. Manuf. Technol.*, 2016, **85**, p 9–12
9. B. Sushovan, D. Hrishikesh, P.T. Kumar et al., Characterization of Intermetallics in Aluminum to Zinc Coated Interstitial Free Steel Joining by Pulsed MIG Brazing for Automotive Application, *Mater. Charact.*, 2016, **112**, p 229–237
10. M.J. Zhang, G.Y. Chen, Y. Zhang et al., Research on Microstructure and Mechanical Properties of Laser Keyhole Welding-Brazing of Automotive Galvanized to Aluminum Alloy, *Mater. Des.*, 2013, **45**(6), p 24–30

11. H. Ozaki and M. Kutsuna, Dissimilar Metal Joining of Zinc Coated Steel and Aluminum Alloy Laser Roll Welding, *Weld. Process.*, 2012, <https://doi.org/10.5772/48242>
12. M.J. Torkamany, S. Tahamtan, and J. Sabbaghzadeh, Dissimilar Welding of Carbon Steel to 5754 Aluminum Alloy by Nd:YAG Pulsed Laser, *Mater. Des.*, 2010, **31**(1), p 458–465
13. V. Soundararajan, E. Yarrapareddy, and R. Kovacevic, Investigation of the Friction Stir Lap Welding of Aluminum Alloys AA 5182 and AA 6022, *J. Mater. Eng. Perform.*, 2007, **16**(4), p 477–484
14. S. Meco, S.G. Stewart, W. Norman et al., Effect of Laser Processing Parameters on the Formation of Intermetallic Compounds in Fe-Al Dissimilar Welding, *J. Mater. Eng. Perform.*, 2014, **23**(9), p 3361–3370
15. Y.B. Chen, S.H. Chen, L.Q. Li et al., Influence of Interfacial Reaction Layer Morphologies on Crack Initiation And Propagation in Ti/Al Joint by Laser Welding-Brazing, *Mater. Des.*, 2010, **31**(1), p 227–233
16. R. Qiu, S. Satonaka, C. Iwamoto et al., Effect of Interfacial Reaction Layer Continuity on the Tensile Strength of Resistance Spot Welded Joints Between Aluminum Alloy and Steels, *Mater. Des.*, 2009, **30**(9), p 3686–3689
17. H. Springer, A. Kostka, E.J. Payton et al., On the Formation and Growth of Intermetallic Phases During Inter Diffusion Between Low-Carbon Steel and Aluminum Alloys, *Acta Mater.*, 2010, **59**(4), p 1586–1600
18. X.M. Meng, G.L. Qin, Y.H. Su et al., Numerical Simulation of Large Spot Laser Plus MIG Arc Brazing-Fusion Welding of Al Alloy to Galvanized Steel, *J. Mater. Process. Technol.*, 2017, **222**, p 307–314
19. J.L. Song, S.B. Lin, C.L. Yang et al., Effects of Si Additions on Intermetallic Compound Layer of Aluminum-Steel TIG Welding-Brazing Joint, *J. Alloys Compd.*, 2009, **488**(1), p 217–222
20. L.Q. Li, D.J. Liu, Y.B. Chen et al., Electron Microscope Study of Reaction Layers Between Single-Crystal WC Particles and Ti-6Al-4 V After Laser Melt Injection, *Acta Mater.*, 2009, **57**(12), p 3606–3614
21. D. Akbari, M. Farahani, N. Soltani et al., Effect of the Weld Groove Shape and Geometry on Residual Stresses in Dissimilar Butt-Welded Pipes, *J. Strain Anal.*, 2011, **47**(2), p 73–82
22. J.L. Song, S.B. Lin, C.L. Yang et al., Analysis of Intermetallic Layer in Dissimilar TIG Welding-Brazing Butt Joint of Aluminium Alloy to Stainless Steel, *Sci. Technol. Weld. Join.*, 2010, **15**(3), p 213–218
23. A. Mathieu, R. Shabadi, A. Deschamps et al., Dissimilar Material Joining Using Laser (Aluminum to Steel Using Zinc-Based Filler Wire), *Opt. Laser Technol.*, 2007, **39**(3), p 652–661